Functionally important binding site for a volatile anesthetic in a voltage-gated sodium channel identified by X-ray crystallography

David Hollingworth[1 †], Karl F. Herold[2 †], Geoff Kelly[3], Vitaliy B. Mykhaylyk[4], Jiaxin Xiang[2], Donghang Zhang[2], B. A. Wallace[1*], Hugh C. Hemmings Jr[2,5]**

1 School of Natural Sciences, Birkbeck University of London, London, UK

2 Department of Anesthesiology, Weill Cornell Medicine, New York, NY, USA

3 The Medical Research Council Biomedical NMR Centre, The Francis Crick Institute, London, UK

4 Diamond Light Source, Harwell Science and Innovation Campus, Chilton, Didcot, UK

5 Department of Pharmacology, Weill Cornell Medicine, New York, NY, USA

† Contributed equally to the work

Significance

While general anesthesia is an essential medical technique, the mechanisms that contribute to its pleiotropic neurological effects of unconsciousness, amnesia, immobility and analgesia remain incompletely understood. Identification of anesthetic binding sites in critical molecular targets like voltage-gated Na^+ channels is essential to elucidation of the mechanisms involved. Using a combined structural and functional approach, we identify and characterize the first known volatile anesthetic binding site in a voltage-gated ion channel.

Abstract

Volatile general anesthetics are used for inhalational anesthesia in hundreds of millions of surgical procedures annually, yet their mechanisms of action remain unclear. Membrane proteins involved in cell signaling are major targets for anesthetics, and voltage-gated ion channels that mediate neurotransmission, movement, and cognition are sensitive to volatile anesthetics (VAs). In many cases, the effects produced by VAs on mammalian ion channels are reproduced in prokaryotic orthologues, providing an opportunity to investigate VA interactions at high resolution using these structurally simpler prokaryotic proteins. We utilized the bacterial voltage-gated sodium channel (VGSC) NavMs from *Magnetococcus marinus* to investigate its interaction with the widely used VA sevoflurane. Sevoflurane interacted directly with NavMs, producing effects consistent with multisite binding models for VA actions on their targets. We report the identification of one of these interactions at atomic detail providing the first high-resolution structure of a VA bound to a voltage-gated ion channel. The X-ray crystal structure shows sevoflurane binding to NavMs within an intramembrane hydrophobic pocket formed by residues from the voltage sensor and channel pore, domains essential for channel gating. Mutation of the dominant sevoflurane binding-site residue within this pocket, and analogous residues found in similar sites in human VGSCs, profoundly affected channel properties, supporting a critical role for this site in VGSC function. These findings provide the basis for future work to understand the role of VA interactions with VGSCs in both the anesthetic and toxic effects associated with general anesthesia.

Keywords: binding site, general anesthesia, mechanism of anesthesia, sevoflurane, voltage-gated sodium channel, X-ray crystallography

Introduction

Since the introduction of diethyl ether as an anesthetic in the 1840s, volatile anesthetics (VAs) have been the primary class of general anesthetics used in clinical practice. Nonflammable halogenated ethers replaced diethyl ether for general anesthesia in the 1960s, and today sevoflurane is the most widely used agent in developed countries due to its improved clinical, pharmacokinetic and environmental properties (1, 2). However, despite their widespread use and critical medical importance, the detailed mechanisms by which VAs produce anesthesia remain unclear.

The neurophysiological actions of VAs include depression of excitatory and enhancement of inhibitory synaptic transmission as a result of direct low-affinity interactions with ligand-gated and voltage-gated ion channels (3–6), which contribute to disruption of neural networks that underlie consciousness, memory and nocifensive movement (7). These membrane proteins are vital to fundamental physiological functions of excitable cells in the nervous system, skeletal muscle and cardiovascular system, and consequently interactions with VAs could also contribute to the serious undesirable effects of VAs including neurotoxicity, cognitive dysfunction, respiratory depression and cardiovascular complications (8–11).

Voltage-gated sodium channels (VGSCs) have been implicated as important targets for the pharmacological effects of VAs (3, 12–17). There are nine human VGSC isoforms (hNavs, Nav1.1 to Nav1.9) which are expressed primarily in excitable tissues (18). These channels cycle through closed, open, fast-inactivated, and slow-inactivated conformational states in a voltage-dependent manner (18). Channel opening produces the upstroke of an action potential which allows propagation of electrical signals, while inactivation closes these channels and influences cellular excitability by controlling channel availability at physiological membrane potentials (18–20). The VAs halothane, isoflurane, desflurane and sevoflurane all disrupt the function of neuronal VGSC subtypes *in vitro* through tonic block and enhanced inactivation (13–15, 21–23), effects that contribute to reduced cellular excitability (24–26) and inhibit presynaptic neurotransmitter release (27–29). Although much is known about the functional effects produced by VAs on VGSCs, the precise pharmacological mechanisms involved require atomic resolution structural data, which have so far remained elusive.

Structural characterization of drug interactions with VGSCs has focused on using bacterial homologues (BacNavs) as surrogates to investigate the molecular basis for the functional effects of drugs on eukaryotic VGSCs. BacNavs are simpler structurally but maintain the basic architecture of their eukaryotic counterparts and share most functional properties. While they only inactivate slowly, and lack the structures required for fast inactivation, slow inactivation is important in controlling channel availability and cellular excitability at physiological membrane potentials (30, 31), and is modulated by VAs (32). Some drugs that affect slow inactivation in mammalian VGSCs also affect fast inactivation, raising the possibility that drugs binding at single sites can modulate both processes (33, 34). The best characterized BacNav, NaChBac from *Bacillus halodurans* (35), is inhibited by VAs at clinical concentrations (36–38), and binding sites have been proposed using molecular dynamics (MD) simulations (37, 39) and non-structural nuclear magnetic resonance (NMR) spectroscopy techniques (40). However, NaChBac has remained refractory to crystallization and no high-resolution X-ray structures exist to substantiate predicted VA binding sites.

To characterize the interactions of VAs with VGSCs at the atomic level, we used NavMs, a BacNav from *Magnetococcus marinus*. NavMs provides an excellent functional and crystallographic model for understanding the actions of drugs on human Navs (41–43). NavMs has the typical BacNav structure of four identical ~30 kDa monomeric subunits that assemble to form a homotetrameric channel (44). Each subunit consists of 6 transmembrane helices (S1-S6, labelled as 1-6 in Fig. 1*A*) that form channels with the basic structure of four peripheral voltage-sensing domains (VSDs; consisting of helices S1-S4), connected by a linker helix (the S4-S5 helix) to a sodium ion (Na^+) conducting pore module (PM; formed by the S5-S6 helices and their interconnecting loops from all four subunits) in a domain-swapped arrangement that leads to the VSD from one subunit packing against the PM from the adjacent subunit (45) (Fig. 1*B*). Movement of arginine residues in the S4 helix of the VSD in response to voltage changes produces conformational changes in the PM through induced structural changes in the S4-S5 linker, resulting in the transition between closed and open channel states. Lateral fenestrations in the pore module form intramembrane structures that connect the membrane to the channel pore and provide access for hydrophobic drugs that can tonically block channels from the resting, closed state (46). While BacNavs share the fundamental tetrameric architecture of all VGSCs, eukaryotic channels are created from a single amino acid chain (~210 kDa) with four non-identical domains (DI-DIV) replacing the four BacNav subunits to create a pseudo-tetrameric structure.

In this study, we employ NavMs as a model for studying the actions of sevoflurane (Fig.1*C*) on hNavs. At clinically relevant concentrations, sevoflurane interacts with NavMs producing effects that mirror its action on hNavs. Using X-ray crystallography, we identify a sevoflurane binding site within NavMs located on the membrane-exposed side of a hydrophobic intramembranous pocket normally associated with lipid, and demonstrate that the determinant sevoflurane binding site residue (tyrosine 143, Y143) in this pocket is critical for channel function. Conservative mutation of Y143 to phenylalanine, as found at homologous positions in two hNav channel domains, does not affect NavMs function or its sensitivity to sevoflurane. Moreover, molecular docking using the neuronal isoform hNav1.1 *in silico* shows that sevoflurane has the potential to bind in pockets containing these phenylalanine residues in hNavs, which, like Y143 in NavMs, we show to be essential to channel function.

Results

Sevoflurane interacts directly with NavMs

Direct interaction between isoflurane and NaChBac has been detected using proton observed saturation transfer difference nuclear magnetic resonance spectroscopy (^{1}H STD-NMR) (40). This ligand-observed technique is ideal for detecting the low-affinity interactions associated with VA binding to its ion channel targets by reporting attenuation of ligand signals caused by internuclear saturation transfer from selectively irradiated protein to ligand when in close contact (distances <7 Å) (47). We probed for interaction between NavMs and sevoflurane at a clinically relevant aqueous sevoflurane concentration of 0.57 mM (2 MAC; representing twice the 50% effective dose (minimum alveolar concentration), see *Methods*). Selective irradiation of the NavMs ^{1}H signal at −0.5 ppm (ON resonance) resulted in saturation transfer from NavMs to sevoflurane causing a reduction in the intensity of all three sevoflurane ^{1}H signals (Fig. 1*D*, *middle*) that did not occur with irradiation at a control resonance outside the NavMs ^{1}H spectrum (−20 ppm, OFF resonance, Fig. 1*D*, *bottom*)

producing robust time-dependent STD (Fig. 1*D*, *top*) until plateau (STDmax, Fig. 1*E*). No STD was produced in the same experiment performed in the absence of NavMs (Supporting Information Fig. S1), identifying direct interaction between sevoflurane and NavMs.

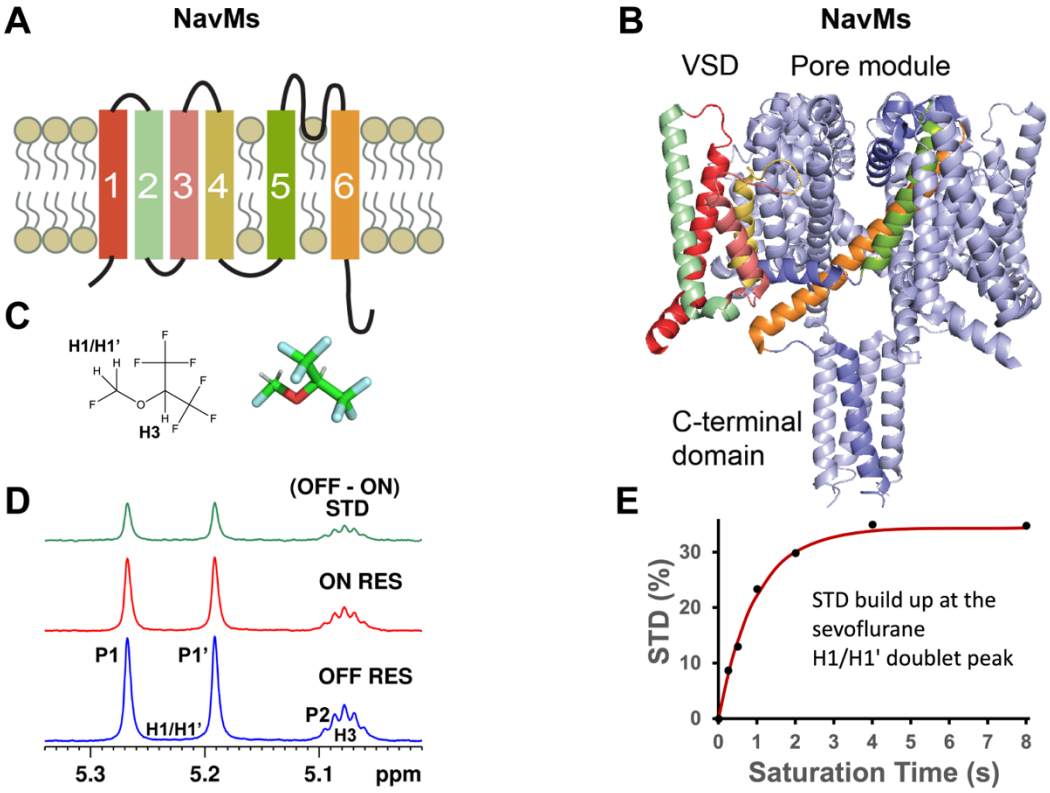

Fig. 1. The homotetramer NavMs interacts with sevoflurane. *(A)* Topology of NavMs in the membrane where 6 transmembrane helices (1-6) make up the monomeric subunit. *(B)* NavMs tetramers form the functional domain-swapped channel with one subunit having colored helices as in *(A). (C)* Sevoflurane structure *(left)* as a chemical drawing with labeling of the three protons *and* in stick representation *(right). (D)* Saturation Transfer Difference (STD) is produced at both sevoflurane proton peaks (P1/P1' formed by the splitting of the H1/H1' peak to give a doublet peak due $^{2}J_{HF}$ coupling with the fluorine of CH_2F-group and P2 formed by H3 as a broad septet peak due to $^{3}J_{HF}$ coupling with the six fluorine atoms of the two neighbouring CF_3-groups*).* Stacked spectra show the STD *(top*, green*)* produced after 4 second saturation at the OFF (*bottom*, blue) and ON (*middle,* red) resonances. (*E*) STD build up is saturation time-dependent until reaching a plateau (STDmax). STD (%) is calculated as (I_off – I_on) / I_off × 100, where I_off and I_on are the integrals of the sevoflurane proton peaks in the OFF RES (irradiation -20 ppm) and the ON RES (-0.5 ppm) spectra at the indicated saturation times. Plot shows STD build up at P1/P1' with the experimental values fit to Equation 1 (see *Methods*).

Sevoflurane binding to NavMs is functionally significant

The functional impact of sevoflurane interaction with NavMs was analyzed by whole-cell patch clamp electrophysiology using human embryonic kidney 293T (HEK293T) cells transiently transfected to express NavMs. An extremely hyperpolarized holding potential (V_h

−180 mV) was required to maintain NavMs in a fully resting state. Transfected cells produced robust Na^+ currents (Fig. 2*A*) allowing measurement of sevoflurane effects on NavMs function. NavMs current (I_{Na}) was tonically blocked by sevoflurane (Fig. 2*A*, 2*B* and 2*D*). Sevoflurane accelerated activation of Na^+ current (Fig. 2*C*) with no significant effect on activation kinetics (Fig. 2*D*), caused a hyperpolarizing shift in steady-state inactivation (Fig. 2*D*, *right*), and slowed recovery from inactivation (Fig. 2*E* and 2*F*, Supporting Information Table 1). This profile of tonic block and modulation of inactivation reflects the effects of VAs observed for hNav subtypes (21) and is consistent with multisite binding models suggested for VA action on VGSCs in MD studies (37, 39, 40). Notably, the hyperpolarizing effect of sevoflurane on channel activation observed in NaChBac (37) was not observed for NavMs or in a previous study on the effects of VAs on hNavs (21).

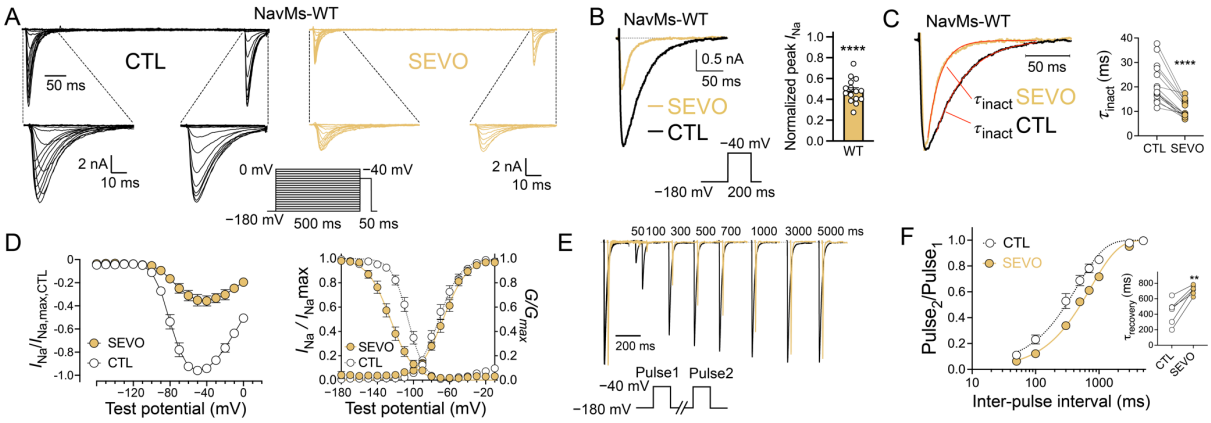

Fig. 2. Sevoflurane inhibits NavMs expressed in HEK293T cells. (*A*) Representative families of whole-cell inward Na^+ currents evoked by the depicted stimulation protocol *(inset*) from a holding potential *(V_h)* of −180 mV in the absence (CTL; *left,* black traces) or presence of 0.57 mM (2 MAC) sevoflurane (SEVO; *right*, gold traces). (*B*) Sevoflurane inhibition of NavMs peak Na^+ current (I_{Na}). Representative traces of peak I_{Na} evoked by a single pulse (*inset*) from a holding potential (V_h) of −180 mV in the absence (CTL; black trace) or presence of sevoflurane (SEVO; gold trace). The normalized peak I_{Na} was reduced to 0.48±0.03 in the presence of 0.57 mM (2 MAC) sevoflurane (****P<0.0001, n=15). (*C*) Sevoflurane decreased the time constant of current decay (τ_{inact}) of channel inactivation. The traces in (*B*) were normalized and data for current decay were fitted to a mono-exponential equation (red curves) to calculate τ_{inact}. Sevoflurane accelerated current decay τ_{inact} by ~2-fold from 21.3±2.0 ms (CTL; white circles, *right* panel) to 10.6±0.9 ms (SEVO; gold circles, ****P<0.0001, n=15). (*D*) Current-voltage relationship of channel activation (I-V curve, *left* panel), normalized conductance (G/G_{max}) and inactivation ($I_{Na}/I_{Na}max$; *right* panel). Sevoflurane did not affect the voltage dependance of half-maximal activation ($V_{½act}$) (−71.5±2.7 mV for CTL; white circles, *vs.* −66.7±2.3 mV for SEVO; gold circles, P=0.0695, n=8). Sevoflurane shifted the voltage dependance of half-maximal inactivation ($V_{½inact}$) by −19.4±2.1 mV toward hyperpolarized potentials (−106±2.2 mV for CTL; white circles, *vs.* −126±2.9 mV for SEVO; gold circles, ****P<0.0001, n=8). (*E*) and (*F*) Sevoflurane slows Na^+ channel recovery from inactivation. A two-pulse protocol was used from a holding potential (V_h) of −180 mV, with two 200 ms test pulses to −40 mV separated by an interpulse interval of 50 to 5000 ms (*inset*). Peak I_{Na} of the second test pulse was normalized to the first ($Pulse_2/Pulse_1$) and plotted against the interpulse interval. Data were fitted to a mono-exponential equation to calculate the time constant τ. (*E*) shows overlaid normalized macroscopic Na^+ current traces of the two pulses with increasing interpulse intervals in the absence (CTL; black traces) or presence (SEVO; gold traces) of 0.57 mM (2 MAC) sevoflurane. The sevoflurane traces were plotted with an *x*-axis offset of +30 ms to allow visual comparison between the two. Peak I_{Na} of the second test pulse recovers more slowly with increasing interpulse intervals in the presence of sevoflurane. (*F*) Fitted data in the absence (CTL; white circles) or presence (SEVO; gold circles) of sevoflurane. *Inset* shows recovery time constants τ derived from the fitted data. Time constant τ increased from 432±64 ms to 714±24 ms in the presence of sevoflurane thereby slowing

recovery from inactivation (**P=0.0023, n=6). Data are mean±SEM; drug effects *vs*. control were tested by paired two-tailed Student's *t*-test (*P<0.05; **P<0.01; ****P<0.0001).

Identification of a sevoflurane binding site in NavMs by X-ray crystallography

No high-resolution structures of a VA bound to a voltage-gated ion channel have been reported. Consequently, the binding sites underlying the reported interactions inferred from NMR, MD simulations, and electrophysiological studies have not been identified. To address this, we utilized NavMs F208L, which we have used in crystallographic investigations of VGSC-drug interactions (41–43) and which crystallizes in the inactivated state (41) targeted by sevoflurane in our functional studies. NavMs F208L is functionally indistinguishable from wild-type (WT) NavMs but crystallizes more consistently yielding higher resolution structures.

We grew apo-NavMs F208L crystals and incubated them with sevoflurane-saturated mother liquor to produce co-crystals of NavMs with sevoflurane (NavMs-SEVO). Crystals were harvested after various incubation times and X-ray diffraction data were collected. Diffraction data were also collected for apo-NavMs crystals processed in the same way under the same conditions but without exposure to sevoflurane. While prolonged incubation periods with sevoflurane led to diminished or no X-ray crystal diffraction, shorter times (<20 min) resulted in some crystals that diffracted to the high resolution apo-NavMs F208L crystals. Comparison of crystals from multiple datasets from apo- and sevoflurane exposed crystals showed that the protein structures were identical (rmsd <0.3 Å) but there was a marked change in the shape of non-protein electron density in a hydrophobic pocket below the S5 helix residue Y143. Apo-crystals had a short, elongated stretch of density attributed to the hydrocarbon tail of lipid or detergent (Fig. 3*A*, *left*), while the electron density in NavMs-SEVO crystals was more ellipsoidal (Fig. 3*A*, *middle*). Sevoflurane could be fit into this density in a number of orientations.

In order to identify this density unambiguously as sevoflurane and better position sevoflurane into this binding site we carried out the same crystal exposure experiments replacing sevoflurane (2-(fluoromethoxy)-1,1,1,3,3,3-hexafluoropropane) with its monochloro-substituted analog 2-(chloromethoxy)-1,1,1,3,3,3-hexafluoropropane (chloroSEVO), which retains anesthetic properties but contains a fluorine to chlorine substitution on the fluoromethyl moiety of sevoflurane (48). Chlorine is a weak anomalous scatterer which can be detected using long-wavelength X-ray crystallography (49). We collected single-wavelength anomalous diffraction (SAD) data on the long-wavelength beamline I23 (Diamond Light Source, Oxford, UK) close to the chlorine absorption K-edge (4.5 keV, 2.755 Å, see methods section). Analysis of data collected on three NavMs-chloroSEVO co-crystals showed the same ellipsoidal density found below Y143 in the electron density map of NavMs-SEVO, with anomalous data showing a signal within this density (Fig. 3*A*, *right*) that overlapped across all three datasets (Supporting Information Fig. S2). This signal was not present in the anomalous data collected from apo-crystals. This identified the chlorine of chloroSEVO, confirming sevoflurane binding to this site in our original data and allowing the correct positioning of chloroSEVO and sevoflurane into the binding site (Fig. 3*B* and 3*C*).

Sevoflurane binds in a hydrophobic intramembrane pocket on the membrane-facing surface of NavMs (Fig. 3*C* and 3*D*) making multiple hydrophobic contacts with V23, G26, and A27 from helix S1 and V107 and L110 from helix S4 of the VSD of one domain, and with T139, V140 and Y143 from the S5 helix of the PM from the following domain (Fig. 3*C* boxed). Y143 makes extensive contacts with sevoflurane identifying it as the determinant binding residue within the binding site. No structural rearrangements occurred on sevoflurane binding at this site. Sevoflurane displaces the aliphatic tail of a lipid (or detergent that can replace lipid during purification) to fill an intramembrane hydrophobic pocket, disrupting the protein-lipid environment which might be required for normal function (50). This pocket would be dynamic *in vivo* as the S4 helix moves in response to depolarization between resting and non-resting states and therefore the sevoflurane binding site found in our inactivated channel structure would not be available in resting channels.

The highest resolution structures of apo-NavMs and NavMs-SEVO (both reported at a resolution of 2.2 Å) were deposited in the Protein Data Bank (apo-NavMs PDB ID: 9GTQ, NavMs-SEVO PDB ID: 9GV1).

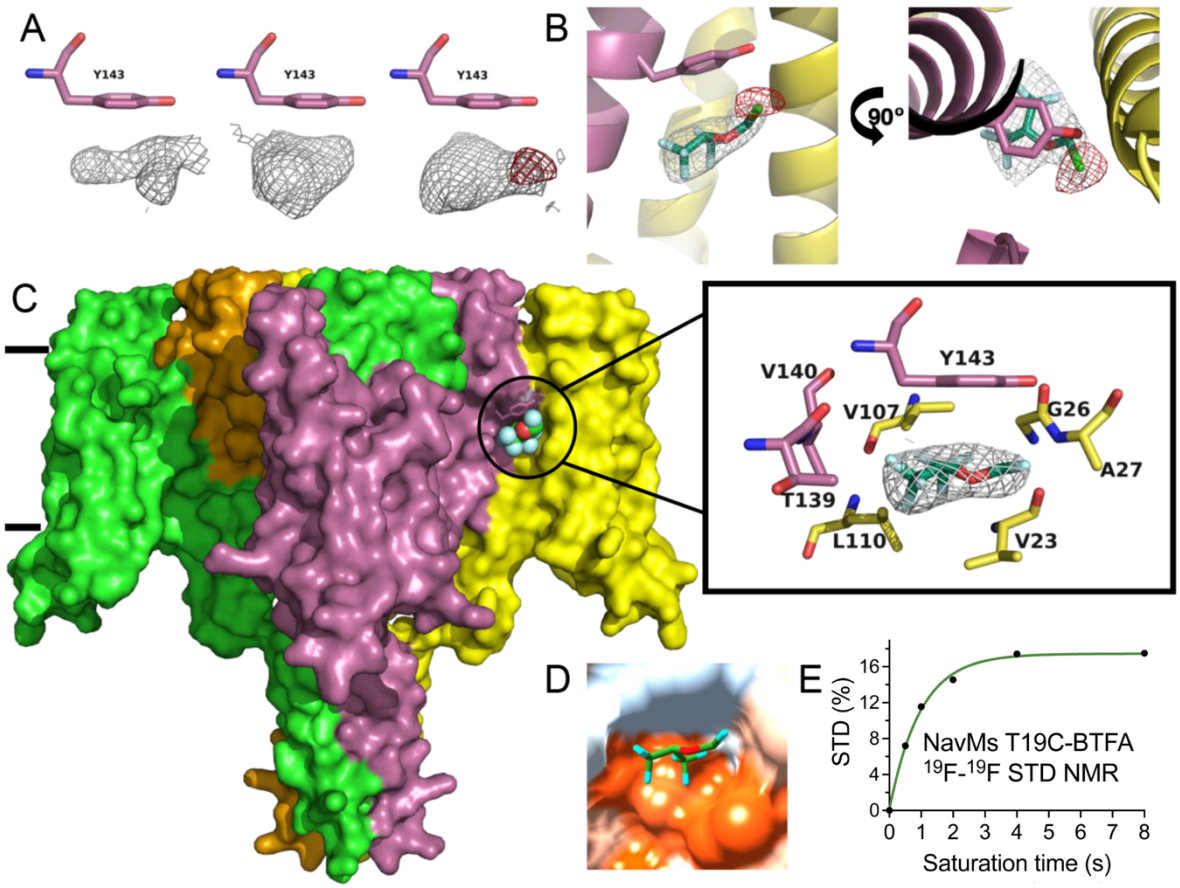

Fig. 3. Sevoflurane binds to NavMs displacing lipid at a membrane exposed site. (*A*) Polder OMIT map density (contour level 4σ) showing the changes in the morphology of electron density (grey) below the helix S5 residue Y143 in apo-crystals (*left*), sevoflurane co-crystals (*middle*) and chloroSEVO crystals (*right*, also showing the anomalous signal for chlorine in chloroSEVO crystals (red) at 4σ. (*B*) Two views of chloroSEVO (stick representation in grey electron density contoured at 1σ) in its binding site located between the S1 and S4 helices of one subunit of NavMs (yellow) and

the S5 helix from the next subunit (magenta). Anomalous chlorine electron density (red, 4σ) allows for accurate positioning of chloroSEVO into the density. (*C*) Space filling model (*left*, colored by subunit) showing sevoflurane (sphere representation) in its intramembrane binding site below Y143 (membrane boundaries indicated with black lines on *left* side of image). Close-up of the sevoflurane binding site (*right inset*) showing residues (colored by subunit) involved in binding to sevoflurane (stick) with sevoflurane electron density contoured at 1σ. (*D*) Hydrophobic surface representation of sevoflurane (stick) bound in the hydrophobic intramembrane pocket of NavMs created by the binding site residues (colored by hydrophobicity red - highest to blue - lowest). (*E*) ^{19}F-^{19}F STD build up curve at the sevoflurane fluorine resonance (−74.7 ppm) shows the relevance of the site for sevoflurane binding at the clinically relevant concentration 0.57 mM (2 MAC) used. STD (%) is calculated as (I_off – I_on) / I_off × 100, where I_off and I_on are the integrals of the sevoflurane fluorine peak at −74.7 ppm in the OFF RES spectrum (where irradiation is at 0 ppm, empty of fluorine signal) and the ON RES spectrum (where irradiation is at −83.8 ppm, which contains the unique fluorine signal from BTFA-labeled NavMs T19C) at the indicated saturation times. Curve produced from experimental values fit using Equation 1 (see *Methods*).

Interestingly, this site was not identified in any of the studies that used MD simulation of potential VA binding sites within VGSCs (37, 39), and therefore no investigation of the functional relevance of this site has been performed.

Sevoflurane interaction at the Y143 binding site occurs at clinical a concentration

The crystal structure of sevoflurane bound to NavMs was determined under conditions of unknown sevoflurane concentration. To determine whether the Y143 site is relevant for sevoflurane binding at the clinically significant concentration used in our functional studies, we employed a fluorine-modified STD NMR technique (^{19}F-^{19}F STD NMR) in which proteins are selectively fluorinated at cysteine residues introduced near predicted binding sites to report on fluorinated ligand interactions exclusively at these sites. This technique has been used to investigate isoflurane binding to NaChBac at clinically important concentrations (40). WT NavMs contains one native cysteine residue, which we mutated to alanine (C52A) prior to incorporating the T19C mutation to make NavMs C52A/T19C. We chose to mutate and modify T19 because the fluorinated probe introduced at this position would be too far away to report on any of potential VA binding sites previously proposed for NaChBac, but only ~6 Å from sevoflurane in the Y143 binding site determined from the NavMs-SEVO crystal structure.

NavMs C52A/T19C expression was extremely low (~15x lower compared to WT NavMs), but the gel filtration profile obtained during purification was like that of WT NavMs, indicative of an equally well-folded protein. Fluorination was performed using the cysteine-specific alkylating agent 3-bromo-1,1,1-trifluoroacetone (BTFA) which conjugates a trifluoromethyl-containing group onto free cysteines. Selective irradiation of the trifluoromethyl resonance of BTFA-labelled NavMs C52A/T19C (at −83.8 ppm) incubated with 0.57 mM sevoflurane produced time-dependent STD build up at the two sevoflurane fluorine resonance peaks (−74.7 ppm, Fig. 3*E)*, representing the six equivalent fluorines in the hexafluoroisopropyl group of sevoflurane, and −152.2 ppm representing the single fluorine in its fluoromethyl group), indicating sevoflurane interacts with this binding site at this clinically relevant concentration. STDmax produced at the ^{19}F peak of the hexafluoroisopropyl group fluorine resonance was much greater (17.5%, Fig. 3*E*) compared to that produced by the fluorine in the fluoromethyl group (3.5%, Supporting Information Fig. S3). This would be expected from

the position of sevoflurane in the NavMs-SEVO crystal structure where the fluorine atoms in the hexafluoroisopropyl group of sevoflurane can be >3 Å nearer to T19 than the fluoromethyl fluorine.

Y143 is critically important to channel function

To investigate the role of Y143 in channel function and sevoflurane binding, we made the tyrosine to alanine substitution Y143A, predicted to abrogate sevoflurane binding at the identified site, in both NavMs and NavMs F208L. Both mutants expressed well and purified like WT NavMs. Crystallization trials using NavMs F208L/Y143A produced crystals, but these did not diffract, and we could not improve this. We compared sevoflurane interaction with NavMs Y143A and WT NavMs using ^{1}H STD NMR. The results showed that NavMs Y143A produced significantly lower STDmax compared to NavMs WT (shown for the P1-P1' doublet peak in Fig. 4*A*), consistent with theY143A mutation attenuating binding.

To examine the functional implications of the Y143A mutation we performed whole cell patch-clamp electrophysiology on HEK293T cells expressing NavMs Y143A. The Y143A mutation led to impaired channel function reflected in small I_{Na} (Fig. 4*B*, *left*). This mutation also produced an extreme negative shift in the steady-state inactivation curve such that a fraction of NavMs Y143A channels did not attain the resting state needed for subsequent activation-dependent experiments even at the extremely hyperpolarized holding potential (V_h) of −180 mV used for our experiments (Fig. 4*C*), with this population of non-activatable channels contributing to the low I_{Na} produced by NavMs Y143A expressing cells. This mutation had no effect on voltage-dependent activation compared to the WT channel (Fig. 4*C*, Supporting Information Table S1).

Sevoflurane at 0.57 mM (2 MAC) almost completely inhibited the already small I_{Na} of NavMs Y143A (Fig. 4*D*). Using a lower sevoflurane concentration of 0.28 mM (1 MAC) we found that sevoflurane inhibited peak I_{Na} and accelerated current decay (Figs. 4*E* and 4*F*, Supporting Information Table S1). However, while, it was possible to determine sevoflurane effects on peak I_{Na} induced by a single pulse on NavMs Y143A, sevoflurane effects on the more complex voltage-dependence of activation or steady-state inactivation could not be reliably determined using this mutant channel due to the extremely low current amplitudes in the presence of sevoflurane. Surprisingly, sevoflurane produced greater relative inhibition of peak I_{Na} with NavMs Y143A compared to WT NavMs (Figs. 4*D* and 4*E, right* panels) even though the mutation attenuates binding. A plausible explanation for this is that sevoflurane-induced stabilization of the inactivated state of NavMs Y143A (as seen with WT NavMs, but which, as mentioned above, could not be practically measured using NavMs Y143A), would further increase the population of activation-resistant NavMs Y143A channels at our holding membrane potential (V_h −180 mV, the practical limit of our equipment). This would result in inhibition of I_{Na} due to the combination of reduced channel availability and tonic block, in contrast to WT NavMs where only tonic block is measured since all channels are in the resting state and available for activation (Fig, 2*D*, *right*).

While we were unable to reliably determine the functional consequences of removing sevoflurane interaction at the Y143 pocket using Y143A, the data clearly demonstrate that Y143 is crucial for normal channel function.

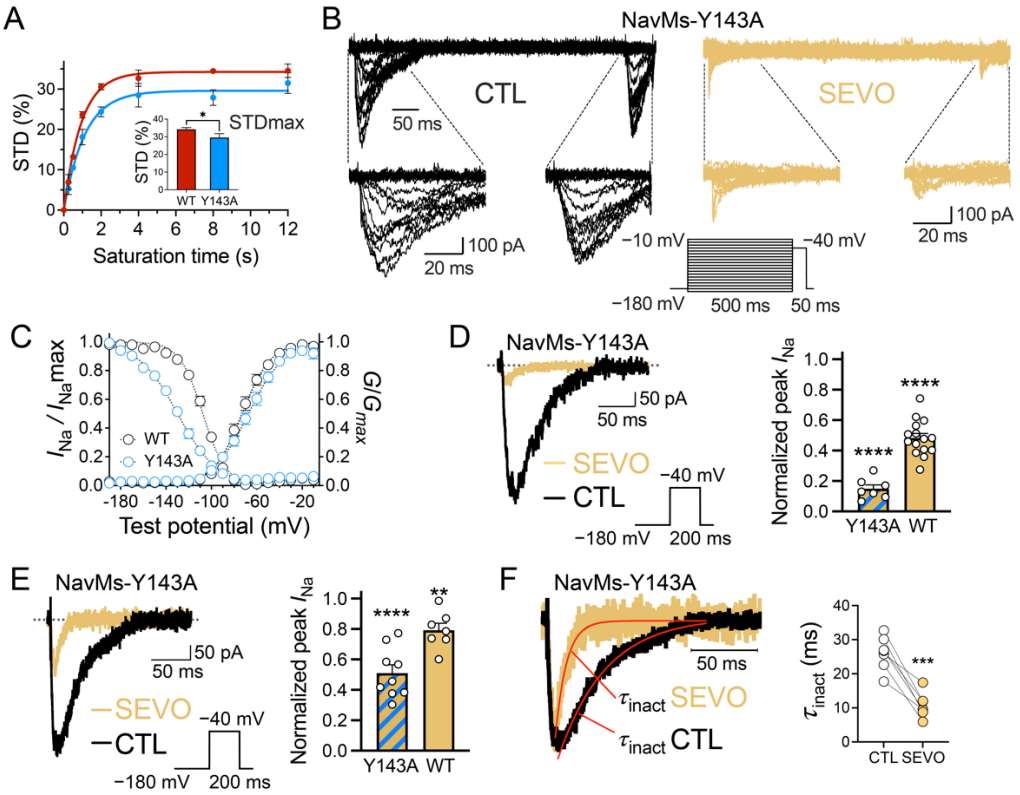

Fig. 4. NavMs Y143A affects sevoflurane binding to NavMs and severely disrupts channel function. (*A*) STD build up curves produced at the proton P1/P1' resonances with 0.57 mM (2 MAC) sevoflurane in the presence of WT NavMs (red) and NavMs Y143A (blue). Y143A had a reduced STDmax (%) compared to WT (*inset*, Y143A 29.6±2.3, WT 34.2±0.93, *P<0.05, unpaired two-tailed Student's *t*-test, n=3). Curves produced from experimental values fit using Equation 1 (see *Methods*). (*B*) Effects of sevoflurane on NavMs Y143A function. Representative families of whole-cell inward Na^+ currents evoked from a holding potential (V_h) of −180 mV in the absence (CTL; *left*, black traces) or presence of a reduced sevoflurane concentration of 0.28 mM (1 MAC) (SEVO; *right*, gold traces); the stimulation protocol is shown in the *inset*. Due to poor expression and small currents for NavMs Y143A, sevoflurane resulted in further reduction of Na^+ current precluding reliable determination of the voltage-dependence of activation and inactivation in the presence of sevoflurane (except for peak I_{Na} from a single pulse, see 4*D-F*). (*C*) Comparison of voltage-dependence of activation and inactivation for NavMs WT and Y143A without sevoflurane. Current-voltage relationship of channel activation (normalized conductance; G/G_{max}) and inactivation (I_{Na}/I_{Na}max). There was no difference in channel activation between WT and Y143A (−72.6±2.1 mV for WT, white circles, G/G_{max}; *vs.* −67.4±2.4 mV for Y143A, blue circles; P=0.113; n=14-15). There was a ~22 mV shift in the voltage-dependence of inactivation for NavMs Y143A compared to NavMs WT (−108±1.4 mV for WT, white circles, I_{Na}/I_{Na}max; *vs.* −130±2.2 mV for Y143A, blue circles; ****P<0.0001, n=14-15). (*D*) Sevoflurane strongly inhibits NavMs Y143A peak I_{Na}. Overlaid macroscopic Na^+ current traces for NavMs Y143A in the absence (CTL; black trace, *left* panel) or presence (SEVO; gold trace) of sevoflurane (*inset* shows stimulation protocol). Normalized peak I_{Na} was reduced to 0.15±0.03 in the presence of 0.57 mM (2 MAC) sevoflurane (*right* panel, ****P<0.0001, n=7; NavMs WT data from Fig. 2*B* included for comparison). Due to near complete block of Na^+ current it was not possible to determine parameters such as voltage-dependence of activation or inactivation. (*E*) Overlaid traces of NavMs Y143A in the absence (CTL; black trace, *left* panel) or presence (SEVO; gold trace) of a reduced sevoflurane concentration of 0.28 mM (1 MAC). Sevoflurane reduced normalized peak I_{Na} for NavMs-Y143A to 0.51±0.05 (****P<0.0001, n=9), and to 0.79±0.05 (**P=0.0038, n=7) for NavMs WT (*right* panel). (*F*) Sevoflurane accelerates the

time course of NavMs Y143A current decay (τ_{inact}). Traces from 4*E* resulting from a single pulse (*inset*; stimulation protocol) were overlaid and normalized to compare current decay. Data for current decay were fitted to a mono-exponential equation (red curves) to calculate τ_{inact}. Sevoflurane accelerated NavMs Y143A τ_{inact} from 26.1±1.8 ms (CTL; white circles) to 10.7±1.9 ms (SEVO; gold circles, ***P=0.0003, n=7; *right* panel). Data are mean±SEM; drug effects *vs*. control were tested by paired (or unpaired for comparison between WT and Y143A) two-tailed Student's *t*-test; (*P<0.05, **P<0.01; ***P<0.001; ****P<0.0001).

The humanized NavMs Y143F channel behaves like wild-type

The Y143 residue is absolutely conserved in all BacNavs consistent with its important role in channel function. All hNavs isoforms contain conserved phenylalanine residues at cognate positions in the S5 helices of domains II and IV (e.g. F902 and F1682 of hNav1.1). To study the consequences of this residue for channel function and sevoflurane binding, we mutated Y143 to phenylalanine in NavMs F208L, creating NavMs F208L/Y143F, which expressed similarly to NavMs F208L and purified identically. It produced crystals under the same conditions as NavMs F208L that diffracted to high resolution producing electron density maps and structures identical to those of NavMs F208L, except for the lack of density associated with the Y143 hydroxyl group. X-ray diffraction data obtained from crystals after co-incubation of NavMs F208L/Y143F with sevoflurane produced electron density maps that showed the same ellipsoidal density below F143 as seen below Y143 in NavMs-SEVO crystals, indicating sevoflurane binding (Fig. 5*A*). Whole cell patch-clamp electrophysiology on HEK293T cells expressing NavMs Y143F showed that this channel behaved like WT NavMs (Fig. 5*B*-5*E*), with sevoflurane producing similar effects on both channels (Fig. 5*B*-5*E*).

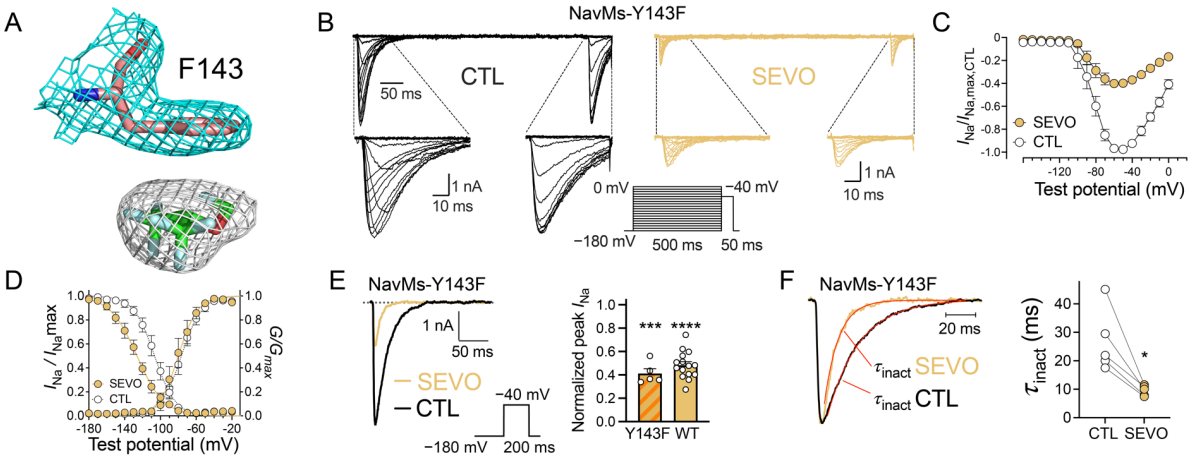

Fig. 5. Humanized NavMs Y143F behaves similarly to wild-type NavMs in function and susceptibility to sevoflurane. (*A*) Co-crystals of NavMs Y143F and sevoflurane show identical sevoflurane density to that found in NavMs-SEVO crystals. (*B*) Representative families of whole-cell inward Na^+ currents in HEK293T cells expressing NavMs Y143F (*inset* shows stimulation protocol) from a holding potential (V_h) of −180 mV in the absence (CTL; black traces) or presence of 0.57 mM (2 MAC) sevoflurane (SEVO; gold traces). (*C*) and (*D*) Current-voltage relationships of channel activation (*I-V* curve, C), normalized conductance (G/G_{max}) and inactivation (I_{Na}/I_{Na}max, *D*). Sevoflurane did not affect the voltage-dependence of activation (−76.7±4.0 mV for CTL; white circles, G/G_{max}; *vs*. −79.6±4.4 mV for SEVO; gold circles, P=0.544, n=5). Sevoflurane shifted the voltage-dependence of half-maximal inactivation ($V_{½inact}$) by −19.5±5.1 mV (−107±3.6 mV for CTL; white circles, I_{Na}/I_{Na}max; *vs*. −126±3.6 mV

for SEVO; gold circles, *P=0.0305, n=5). (*E*) Sevoflurane inhibits both NavMs Y143F and WT NavMs peak Na^+ current (I_{Na}). Representative overlaid traces of Na^+ currents evoked by a single pulse (*inset* shows stimulation protocol) from V_h −180 mV in the absence (CTL; black trace, *left* panel) or presence of sevoflurane (SEVO; gold trace). Normalized peak I_{Na} was reduced to 0.41±0.04 in the presence of 0.57 mM (2 MAC) sevoflurane (*right* panel; ***P=0.00014, n=5). NavMs WT data from Fig. 2B included for comparison (*right* panel). (*E*) Sevoflurane increases the time course of current decay (τ_{inact}) of channel inactivation in NavMs Y143F and WT NavMs. The traces in (*D*) were normalized and data for current decay were fitted to a mono-exponential equation (red curves) to calculate τ_{inact}. Sevoflurane accelerated current inactivation τ_{inact} from 26.8±5.0 ms (CTL; white circles; *right* panel) to 9.6±0.8 ms (SEVO; gold circles, *P=0.0172, n=5). Data are mean±SEM; drug effects *vs*. control were tested by paired two-tailed Student's *t*-test; (*P<0.05; ***P<0.001).

Sevoflurane binding to cognate pockets in human Nav1.1

Because NavMs and NavMs Y143F channels were similar functionally and in their responses to sevoflurane, we investigated whether the phenylalanine-containing pockets in hNavs preserves sevoflurane binding and inhibition. To investigate binding at these sites we used molecular docking simulations. As proof of principal, we docked sevoflurane into the NavMs Y143 site *in silico*. The top hit from the docking simulation produced a binding position for sevoflurane that closely matched that of the crystal structure (Fig. 6*A*) with an estimated binding energy of −4.5 kcal/mol, indicative of the weak interaction characteristic of sevoflurane binding to its targets. We performed the same docking experiment for the two predicted binding pockets of hNav1.1 (DI-DII containing F902 and DIII-DIV containing F1682) using the cryoEM hNav1.1 structure (PDB ID: 7DTD, inactivated state) (51). Sevoflurane docked into both pockets with the top hit for each simulation (Fig. 6*B* and 6*C*) showing sevoflurane could fit and bind in these pockets with binding poses that overlapped with sevoflurane in the NavMs-SEVO structure (Supporting Information, Fig. S4). Similarly to NavMs, these simulations produced sevoflurane binding to these sites with weak affinities (top binding energies; DI-DII 4.1 kcal/mol, DIII-DIV 5.3 kcal/mol).

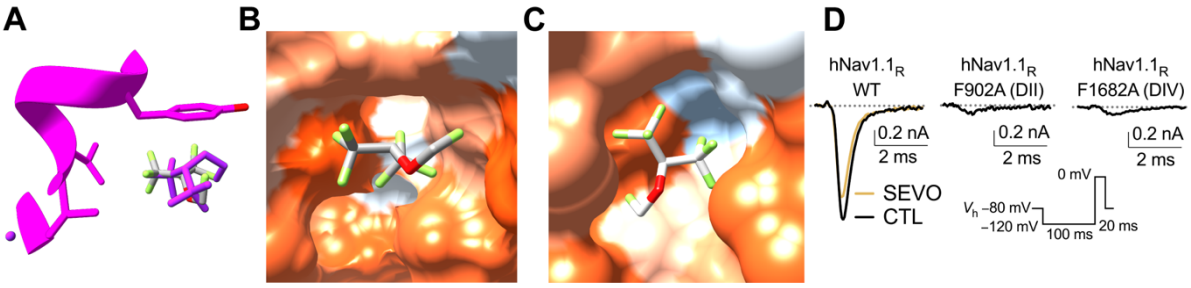

Fig. 6. Sevoflurane interaction with human Nav1.1. (*A*) Molecular docking simulation of sevoflurane and NavMs near the Y143 binding pocket produces top poses that overlay with that of sevoflurane bound in the X-ray crystal structure. Image shows the top binding pose of sevoflurane from the simulation (stick, colored by heteroatom) overlapping closely with sevoflurane bound in the NavMs-SEVO co-crystals (magenta). (*B*) Top pose from molecular docking simulation showing sevoflurane (stick, colored by heteroatom) can bind in the DI-DII pocket of hNav1.1. (*C*) Top pose from molecular docking simulation showing sevoflurane (stick, colored by heteroatom) can bind in the DIII-DIV pocket of hNav1.1. (*D*) $hNav1.1_R$ transiently expressed in the mammalian neuronal ND7/23 cell line produced strong tetrodotoxin-resistant Na^+ current (black trace, *left* panel) that was tonically inhibited by 0.57 mM (2 MAC) sevoflurane (gold trace, *left* panel). F902A and F1682A mutations introduced into $hNav1.1_R$ abolish channel function (F902A, *middle* and F1682A, *right*). With *inset* showing stimulation protocol.

In contrast to the homotetrameric NavMs structure, the single chain hNav1.1 structure allows for single residues of individual domains to be selectively mutated. We studied the functional effects of single F902A (in DII) and F1682A (in DIV) mutations in tetrodotoxin (TTX)-resistant hNav1.1 expressed in rodent ND7/23 neuroblastoma cells that support functional hNav expression and isolation of Nav currents (52–54). Modification of hNav1.1 to be resistant to TTX (F383S, referred to as hNav1.1$_R$) (55) allowed recordings of hNav1.1 currents in isolation of natively expressed Na^+ currents which are completely blocked by 250 nM TTX in this cell line. hNav1.1$_R$ produced a strong TTX-resistant Na^+ current that was inhibited by sevoflurane (Fig. 6*D*, *left*). However, expression of the mutant channels produced no TTX-resistant Na^+ current, indicating that the individual F902A and F1682A mutations completely abolished hNav1.1 currents (Fig. 6*D*, *middle* and *right*). Therefore, F902 and F1682 are each critical for hNav1.1 function, with mutation to alanine eliminating current, precluding further functional studies to elucidate the importance of sevoflurane binding to these sites in human channels.

Discussion

We show that sevoflurane modulates NavMs function producing effects that closely resemble those observed in mammalian VGSCs, and we present the first atomic resolution structure of a volatile anesthetic bound to a voltage-gated ion channel. These findings establish NavMs as an excellent model for studying the structure-function relationships between VAs and VGSCs. The VAs sevoflurane, isoflurane, desflurane, and halothane have similar effects on human VGSCs: tonic block from the resting state, accelerated current decay, hyperpolarized voltage-dependence of steady-state inactivation, and slowed recovery from inactivation without affecting activation (21); we show that sevoflurane affects NavMs similarly. The X-ray crystal structure of NavMs bound to sevoflurane presented here represents the first structure involving a VA interaction with a voltage-gated ion channel and the first structure of any protein bound to sevoflurane in the Protein Data Bank (PDB). This site was independently validated by data obtained by NMR spectroscopy which show that sevoflurane interaction with this pocket occurs at a clinically relevant concentration in the WT channel and that the Y143A mutation abolishes this interaction. This will facilitate further studies into how VA binding to this and other sites on VGSCs contribute to the functional effects of VAs on ion channels.

The identified interaction between sevoflurane and NavMs reveals binding at a membrane exposed hydrophobic intramembrane surface cavity where binding displaces bound lipid. This suggests two potential mechanisms for VA action at this site: functional effects due to direct VA binding and/or indirect effects caused by displacement of critical lipids necessary for normal channel function. This interaction is especially interesting as sevoflurane binds to a pocket that is formed only when the S4 voltage sensing helix is positioned in its outward (non-resting) conformational state, with the functional significance of this site revealed by the disruptive effects on function caused by Y143A mutation of NavMs, and the lethal effects caused by F902A and F1682A mutation at cognate sites identified in hNav1.1.

This study provides a paradigm to match specific binding events to the functional effects produced by VA binding to human VGSCs with the goal of elucidating the molecular mechanisms that contribute to both anesthesia and anesthetic-induced side effects. Identification of these mechanisms is critical to further improvements in the design and development of novel anesthetics using high throughput screening and structure-activity studies of VGSC anesthetic binding sites (56, 57).

Data availability

The atomic coordinates and crystallographic structure factors generated for Apo-NavMs and NavMs complexed with sevoflurane (NavMs-SEVO) have been deposited in the protein data bank (PDB) under the accession codes 9GTQ for Apo-NavMs [PDB DOI: **https://doi.org/10.2210/pdb9gtq/pdb**] and 9GV1 for NavMs-SEVO [PDB DOI: **https://doi.org/10.2210/pdb9gv1/pdb**] with data collection and refinement statistics details provided in Supporting information Table 2. The PDB code of the previously published structures used in this study are for NavMs 6SX5 [**https://doi.org/10.2210/pdb6sx5/pdb**] and for Nav1.1 7DTD [**https://doi.org/10.2210/pdb7dtd/pdb**]. Source data for NMR and electrophysiology are provided as a separate data file.

Acknowledgements

We thank the staff of Diamond Light Source (data obtained under proposal MX23853), the European Synchrotron Radiation Facility (Grenoble, France; data obtained under proposals MX2415 and MX2606) and EMBL (P13 DESY, Hamburg, Germany; data obtained under proposal MX842) for assistance and support on the beamlines used in this study. We thank Frances Thomas for aid with some of the images used in this study.

Funding

US National Institutes of Health grant R01 GM58055 to HCH, a *British Journal of Anaesthesia* International Collaborative Grant to HCH and KFH, and a Rosetrees grant (ref: CF2\100001) to BAW. This work was also supported by the Francis Crick Institute through the provision of access for DH and BAW to the MRC Biomedical NMR Centre, which is funded by Cancer Research UK (CC1078), the UK Medical Research Council (CC1078), and the Wellcome Trust (CC1078).

Author contributions

HCH, KFH and BAW conceived the project; DH and KFH designed the research; DH performed the molecular biology, protein expression and purification and chemical modifications for the structural studies; GK and DH performed and analyzed NMR spectroscopy; DH performed and analyzed X-ray crystallography; VBM and DH performed and analyzed the long-wavelength X-ray crystallography; KFH performed the molecular biology, cell culture and electrophysiology using NavMs; JX and DZ performed the electrophysiology using hNav1.1; DH and KFH wrote the paper under the supervision of BAW and HCH.

495

496 **Conflicts of interest**

497 HCH is editor-in-chief of the *British Journal of Anaesthesia* and receives royalties from
498 Elsevier. The other authors have no conflicts to declare.

499

500 Methods

501 Molecular biology

502 Site-directed mutagenesis of the NavMs DNA sequence contained within the pET-15b plasmid
503 vector was performed to create the mutants described in this study (Quikchange, Agilent), with
504 the primers listed in Supporting information Table S3. Plasmids generated were chemically
505 transformed into NEB® 5-alpha competent *E. coli* (New England Biolabs) and mutation
506 verified by automated DNA sequencing (Eurofins Genomics) before transformation of correct
507 plasmids into Overexpress™ C41(DE3) Chemically Competent *E. coli* cells (Lucigen) for
508 protein expression.

509 Protein expression and purification

510 NavMs proteins were expressed in C41(DE3) *E. coli* cells grown in Luria Broth containing 100
511 µg/ml ampicillin, in shaking flasks at 37ºC. To induce NavMs protein expression, when the
512 cells reached an optical density (OD600) of 0.8, 0.5 mM IPTG was added followed by further
513 incubation for 3.5 h. Cell pellets were resuspended in 20 mM Tris pH 7.5, 150 mM NaCl, 1 mM
514 $MgCl_2$ and cells were broken by pressure. Cell debris was removed by centrifugation at
515 20,000x*g* for 30 min and the resulting supernatant was spun at 195,000x*g* for 2 h to pellet
516 membranes. Protein was extracted from the membranes using a buffer containing 20 mM Tris,
517 pH 7.5, 300 mM NaCl, 20 mM imidazole and 1.5% DDM (Anatrace) on a rotating shaker at
518 4ºC for 2 h. Solubilized proteins were loaded onto a 1 ml HisTrap HP column (Cytiva Life
519 Sciences) which was washed, and detergent was exchanged on the column with buffer
520 containing 20 mM Tris–HCl, pH 7.5, 300 mM NaCl, 50 mM imidazole and 0.52% HEGA-10
521 (Anatrace) prior to protein elution using the same buffer with 1 M imidazole. The eluate volume
522 was reduced and imidazole concentration lowered to ~50 mM by sequential adding of buffer
523 without imidazole using a 100 kDa cut-off concentrator (Amicon). NavMs proteins were treated
524 with thrombin protease (Merck) for 16 h at 4°C then purified by size exclusion chromatography
525 using a Superdex 200 10/300 column (Cytiva Life Sciences). NavMs was concentrated to
526 10 mg/ml and either used directly or stored at −80°C. NavMs mutants were concentrated to
527 10 mg/ml accounting for the different extinction coefficients caused by mutation.

528 BTFA-labelling

529 Following purification, NavMs C52A/T19C protein was diluted to 10 µM. 5 mM BTFA (Merck)
530 was added, and the mixture was incubated at 4°C for 24 h with gentle rotation. Free BTFA
531 was removed from protein by gel filtration using a Superdex 200 10/300 column and gave a
532 protein peak identical in elution volume when compared to untreated protein. Complete
533 removal of the probe was confirmed by lack of a sharp peak at the BTFA fluorine resonance
534 in the 1D 19F NMR spectrum of the NavMs-BTFA sample.

535 ## Sevoflurane preparation

536 Sevoflurane concentrations used an aqueous concentration of 0.57 mM corresponding to
537 twice the minimum alveolar concentration (2 MAC), where MAC (in vol%) is the concentration
538 needed to prevent movement in 50% of subjects in response to a painful stimulus (comparable
539 to the ED_{50}).

540 ## Structural techniques

541 *Saturation Transfer Difference Nuclear Magnetic Resonance (STD-NMR)*

542 ^{1}H Experiments were performed with 0.57 mM (2 MAC) sevoflurane in buffer (20 mM Tris-Cl,
543 300 mM NaCl, 0.52% Hega-10) +/− 5 µM NavMs protein. ^{19}F experiments we performed in
544 the same conditions but using 50 µM fluorine-labeled NavMs protein. All STD NMR
545 experiments were performed on a Bruker Biospin Avance IIIHD 700 spectrometer, equipped
546 with a 5 mm TCI cryoprobe, using the acquisition software Topspin 3.5. NMR spectra were
547 acquired by collecting alternating on- and off-resonance spectra with saturation achieved
548 using a train of Gaussian-shaped pulses of 50 ms duration with a peak B1 field of 500 Hz
549 determined over randomised collections at the saturation time point specified. Data were
550 processed in Topspin 3.5 (Bruker) and fitted to the mono-exponential equation:

551 $$STD\ (\%) = STDmax[(1-exp(-ksatt)] \qquad (1)$$

552 where STD(%) = (Voff – Von)/Voff x100. Voff and Von are the peak integrals from the off and
553 on resonance saturation transfer NMR spectra. STDmax represents the STD at the maximal
554 plateaued value.

555 *Crystallography*

556 Crystallization proceeded using stock NavMs F208L (denoted as wild-type; WT) or mutants
557 (10 mg/ml) in sitting drops at 4°C with drops containing 75 nl well condition and 75 nl NavMs
558 dispensed using a mosquito® crystal robot (SPT Labtech). Apo-crystals were grown in well
559 conditions containing 30-35% PEG 300,100 mM HEPES (pH 7) and 0-100 mM NaCl. For
560 NavMs-SEVO crystals sevoflurane was saturated into reservoir solutions of crystal containing
561 wells and incubated with the crystals for up to 1 h with periodic harvesting and flash freezing
562 of individual crystals in liquid nitrogen.

563 *Data Collection and Processing*

564 Crystal optimization was required in this study. X-ray diffraction data were collected for crystals
565 using the beamlines P13 (EMBL, Hamburg, Germany), ID23-1 and ID30A-1 (ESRF, Grenoble,
566 France) and I24 and I04 (Diamond Light Source, Oxford, UK) working at wavelengths between
567 0.886 and 0.9795 Å. Indexing and integration were performed with the XIA2-DIALS pipeline
568 (58, 59), followed by scaling and merging with AIMLESS (60). Molecular replacement was
569 performed with PHASER (61) using the search model (PDB ID: 6SX5) followed by model
570 building in COOT (62) and structure refinement using REFMAC (63). Polder Omit maps were
571 created in Phenix (64). Graphic illustrations were produced using PYMOL (65) and UCSF
572 Chimera (66).

573 *Long Wavelength X-ray Crystallography*

Data were collected on the long-wavelength MX beamline I23 at Diamond Light Source at a wavelength of 2.755 Å (4.5 keV). This wavelength, although not optimal for chlorine (K-edge 4.4 Å, 2.82 keV), was selected as a compromise between the increasing signal from chlorine as it reaches its K-edge and the decreasing data quality that results from increasing X-ray absorption at longer wavelengths. Each dataset consisted of 360° rotation with an exposure time of 0.1 s per 0.1° image. Multiple datasets were taken at varying kappa and phi values to ensure the fidelity of the anomalous signals. Crystallographic data processing was performed as above. Anomalous difference maps were generated using Anode (67).

Electrophysiology

NavMs cDNA Constructs and Cell Culture

The NavMs-pTracer-CMV2 plasmid carrying the separately expressed eGFP gene was used for whole-cell electrophysiology (68). Standard site-directed mutagenesis protocols using the QuikChange Lightning kit (Qiagen, Germantown, MD) were used to create the NavMs Y143A and Y143F mutants. The entire open reading frames of successful cDNA clones were confirmed by Sanger sequencing.

Mammalian HEK293T cells (CRL-3216 from ATCC, Manassas, VA) were maintained in high-glucose Dulbecco's modified Eagle medium supplemented with 10% (vol/vol) fetal bovine serum (FBS), 2 mM GlutaMAX (Life Sciences, Waltham, MA) and 1% penicillin-streptomycin (Life Sciences). Passage numbers between 4 and 30 were used. Cells were seeded into 35-mm dishes and transfected with the respective NavMs cDNA after 1-3 days using Lipofectamine 2000 (Life Sciences) according to the manufacturer's protocol. One day after transfection, cells were released with TrypsinLE (Life Sciences) and replated at lower density onto 12-mm round #1.5 glass coverslips (Warner Instruments, Holliston, MA) a minimum of 3 h before recording isolated adherent cells with eGFP fluorescence.

Human Nav1.1 cDNA Constructs and Cell Culture

Na^+ currents from human neuronal Na_v subtype $Na_v1.1$ were recorded and analyzed by heterologous expression in a neuronal background using the ND7/23 neuroblastoma cell line (53). An optimized version of wild-type human $Na_v1.1$ (accession number NM_001165963) was kindly provided by A. L. George, Jr. (Northwestern University, Evanston, IL) and obtained via AddGene (Watertown, MA) (69). hNav1.1 was rendered TTX resistant by a single mutation (F383S) located in the extracellular toxin binding domain that has been shown to have no effect on gating properties, channel kinetics, or anesthetic sensitivity (25, 55) referred to as $hNa_v1.1_R$. Standard site-directed mutagenesis protocols using the QuikChange Lightning kit (Qiagen, Germantown, MD) were used to create the $hNav1.1_R$ F902A and F1682A mutants. The entire open reading frames of successful cDNA clones were confirmed by Sanger sequencing.

Rodent ND7/23 neuroblastoma cells (Sigma-Aldrich, St. Louis, MO) were plated on 12-mm glass coverslips and incubated at 37°C in a humidified atmosphere of 5% CO_2/95% air in Dulbecco's modified Eagle's medium supplemented with 10% (v/v) fetal bovine serum, 2 mM GlutaMax (Life Sciences), 1% penicillin-streptomycin (Life Sciences). This cell line provides a neuronal background for expression of Na_v by providing critical factors such as auxiliary subunits that facilitate functional expression of the channel protein (53). ND7/23 cells were transfected with 4 µg $hNa_v1.1_R$ cDNA using Lipofectamine LTX (Invitrogen, Carlsbad,

CA). Electrophysiological studies were conducted 24 h after transfection. TTX-resistant Na_v subtypes were studied in the presence of 250 nM TTX to block endogenous Na^+ currents (25, 53).

Whole-cell Patch-clamp Electrophysiology

Pipettes were pulled from standard borosilicate glass (1.5 mm OD/0.86 mm ID; Sutter Instrument, Novato, CA) to a resistance of 3–4 MΩ (when filled) for NavMs or 1.5–2.5 MΩ for $hNav1.1_R$ using a P-1000 puller (Sutter Instrument). Whole-cell voltage-clamp electrophysiology was performed (70) using an AxoPatch 200B amplifier (Molecular Devices, San Jose, CA) connected to a DigiData 1550A analogue-to-digital converter (Molecular Devices). Signals were sampled at 20 kHz and filtered at 5 kHz, respectively. Series resistance was corrected 85–90%. Capacitive current transients were cancelled by the internal amplifier circuitry, and leak currents were subtracted using a standard P/4 protocol applied after the desired stimulus. For NavMs, cells were continuously perfused with extracellular solution at room temperature (24°C) containing (mM) 150 NaCl, 10 Hepes, 1.8 $CaCl_2$ and 1 $MgCl_2$, adjusted to pH 7.4 with NaOH. Pipette solutions contained (mM) 110 CsF, 30 NaCl, 10 Hepes, 5 ethylene glycol tetraaceticacid (EGTA), adjusted to pH 7.30 with CsOH. Osmolality of all solutions were balanced to 300±3 mOsm/kg H_2O with sucrose. For $hNav1.1_R$, cells were continuously perfused with extracellular solution at room temperature (24°C) containing (mM) 130 NaCl, 10 Hepes, 3.25 KCl, 2 $CaCl_2$, 2 $MgCl_2$, 0.1 $CdCl_2$, 20 tetraethylammonium-Cl, 0.00025 tetrodotoxin, and 5 D-glucose adjusted to pH 7.4 with NaOH. Pipette solutions for $hNav1.1_R$ contained (mM) 120 CsF, 10 NaCl, 10 Hepes, 10 ethylene glycol tetraaceticacid (EGTA), 10 tetraethylammonium-Cl, 1 $CaCl_2$, 1 $MgCl_2$ adjusted to pH 7.30 with CsOH. Osmolality of all solutions were balanced to 310±3 mOsm/kg H_2O with sucrose. Saturated sevoflurane (Abbott Laboratories) stock solutions were prepared in extracellular solution in gas-tight glass vials and further diluted in gas-tight Hamilton syringes (Hamilton, Reno, NV) to the desired working concentration. Solutions in gas-tight syringes were delivered using a pressurized perfusion system (ALA Scientific Instruments, Farmingdale, NY) with Teflon tubing via a 200 μm diameter manifold tip positioned ~200–300 μm from the recorded cell. After control recordings, sevoflurane was perfused before subsequent recordings and continuously thereafter until washout. Solutions were delivered through a pressurized perfusion system to minimize mechanical disturbance of cells during sevoflurane superfusion. Mock experiments with extracellular solution showed no effect on I_{Na} (data not shown). Sevoflurane concentrations equivalent to clinically effective concentrations in mammals were 0.28 mM and 0.57 mM, equivalent to 1 or 2 times the minimum alveolar concentration (MAC) (71) after correction to room temperature and were confirmed by gas chromatography (53).

Molecular Docking

Molecular docking was performed using the docking platform Autodock Vina (72) in UCSF Chimera (64). Sevoflurane was docked into a box surrounding the sevoflurane binding site identified in NavMs (PDB ID: 6SX5) and the predicted cognate binding sites in hNav1.1 (PDB ID: 7DTD) using a receptor search volume of 20x20x20 Å and selecting for generation of the top 10 binding modes for each search. Only the top binding mode produced at the sites in NavMs and Nav1.1 are reported here.

660 ## References

661 1. I. Smith, M. Nathanson, P. F. White, Sevoflurane-a long-awaited volatile anaesthetic. *British*
662 *Journal of Anaesthesia* **76**, 435–445 (1996).

663 2. F. McGain, J. Muret, C. Lawson, J. D. Sherman, Environmental sustainability in anaesthesia and
664 critical care. *BJA: British Journal of Anaesthesia* **125**, 680 (2020).

665 3. H. C. Hemmings Jr, *et al.*, Emerging molecular mechanisms of general anesthetic action. *Trends*
666 *Pharmacol Sci* **26**, 503–510 (2005).

667 4. N. P. Franks, Molecular targets underlying general anaesthesia. *Br J Pharmacol* **147 Suppl 1**, S72-
668 81 (2006).

669 5. N. P. Franks, General anaesthesia: from molecular targets to neuronal pathways of sleep and
670 arousal. *Nat Rev Neurosci* **9**, 370–386 (2008).

671 6. H. C. Hemmings Jr, *et al.*, Towards a Comprehensive Understanding of Anesthetic Mechanisms
672 of Action: A Decade of Discovery. *Trends Pharmacol Sci* **40**, 464–481 (2019).

673 7. M. T. Alkire, A. G. Hudetz, G. Tononi, Consciousness and Anesthesia. *Science* **322**, 876–880
674 (2008).

675 8. M. Doi, K. Ikeda, Respiratory effects of sevoflurane. *Anesth Analg* **66**, 241–244 (1987).

676 9. J. C. Belrose, R. R. Noppens, Anesthesiology and cognitive impairment: a narrative review of
677 current clinical literature. *BMC Anesthesiology* **19**, 241 (2019).

678 10. N. Karanovic, *et al.*, The acute hypoxic ventilatory response under halothane, isoflurane, and
679 sevoflurane anaesthesia in rats. *Anaesthesia* **65**, 227–234 (2010).

680 11. M.-A. Neag, A.-O. Mitre, A. Catinean, C.-I. Mitre, An Overview on the Mechanisms of
681 Neuroprotection and Neurotoxicity of Isoflurane and Sevoflurane in Experimental Studies. *Brain*
682 *Research Bulletin* **165**, 281–289 (2020).

683 12. B. P. Bean, P. Shrager, D. A. Goldstein, Modification of sodium and potassium channel gating
684 kinetics by ether and halothane. *J Gen Physiol* **77**, 233–253 (1981).

685 13. B. Rehberg, Y. H. Xiao, D. S. Duch, Central nervous system sodium channels are significantly
686 suppressed at clinical concentrations of volatile anesthetics. *Anesthesiology* **84**, 1223–1233;
687 discussion 27A (1996).

688 14. W. Ouyang, G. Wang, H. C. Hemmings Jr, Isoflurane and propofol inhibit voltage-gated sodium
689 channels in isolated rat neurohypophysial nerve terminals. *Mol Pharmacol* **64**, 373–381 (2003).

690 15. W. OuYang, H. C. Hemmings Jr, Isoform-selective effects of isoflurane on voltage-gated Na+
691 channels. *Anesthesiology* **107**, 91–98 (2007).

692 16. T. Horishita, E. I. Eger, R. A. Harris, Effects of Volatile Aromatic Anesthetics on Voltage-Gated
693 Na+ Channels Expressed in Xenopus Oocytes. *Anesth Analg* **107**, 1579–1586 (2008).

694 17. K. F. Herold, H. C. Hemmings Jr, Sodium channels as targets for volatile anesthetics. *Front*
695 *Pharmacol* **3**, 50 (2012).

18. M. de Lera Ruiz, R. L. Kraus, Voltage-Gated Sodium Channels: Structure, Function, Pharmacology, and Clinical Indications. *J Med Chem* **58**, 7093–7118 (2015).

19. N. Eijkelkamp, *et al.*, Neurological perspectives on voltage-gated sodium channels. *Brain* **135**, 2585–2612 (2012).

20. M.-R. Ghovanloo, K. Aimar, R. Ghadiry-Tavi, A. Yu, P. C. Ruben, "Chapter Fifteen - Physiology and Pathophysiology of Sodium Channel Inactivation" in *Current Topics in Membranes*, Na Channels from Phyla to Function., R. J. French, S. Yu. Noskov, Eds. (Academic Press, 2016), pp. 479–509.

21. W. Ouyang, K. F. Herold, H. C. Hemmings Jr, Comparative effects of halogenated inhaled anesthetics on voltage-gated Na+ channel function. *Anesthesiology* **110**, 582–590 (2009).

22. C. Zhou, K. W. Johnson, K. F. Herold, H. C. Hemmings Jr, Differential Inhibition of Neuronal Sodium Channel Subtypes by the General Anesthetic Isoflurane. *J Pharmacol Exp Ther* **369**, 200–211 (2019).

23. M. Shiraishi, R. A. Harris, Effects of alcohols and anesthetics on recombinant voltage-gated Na+ channels. *J Pharmacol Exp Ther* **309**, 987–994 (2004).

24. W. Ouyang, H. C. Hemmings Jr, Depression by isoflurane of the action potential and underlying voltage-gated ion currents in isolated rat neurohypophysial nerve terminals. *J Pharmacol Exp Ther* **312**, 801–808 (2005).

25. K. Purtell, K. J. Gingrich, W. Ouyang, K. F. Herold, H. C. Hemmings Jr Activity-dependent depression of neuronal sodium channels by the general anaesthetic isoflurane. *British Journal of Anaesthesia* **115**, 112–121 (2015).

26. M. Ou, *et al.*, The General Anesthetic Isoflurane Bilaterally Modulates Neuronal Excitability. *iScience* **23**, 100760 (2020).

27. H. C. Hemmings Jr, W. Yan, R. I. Westphalen, T. A. Ryan, The general anesthetic isoflurane depresses synaptic vesicle exocytosis. *Mol Pharmacol* **67**, 1591–1599 (2005).

28. R. I. Westphalen, J. Yu, M. Krivitski, T.-Y. Jih, H. C. Hemmings Jr, Regional differences in nerve terminal Na+ channel subtype expression and Na+ channel-dependent glutamate and GABA release in rat CNS. *J Neurochem* **113**, 1611–1620 (2010).

29. R. I. Westphalen, K. M. Desai, H. C. Hemmings Jr, Presynaptic inhibition of the release of multiple major central nervous system neurotransmitter types by the inhaled anaesthetic isoflurane. *Br J Anaesth* **110**, 592–599 (2013).

30. Y. Y. Vilin, P. C. Ruben, Slow inactivation in voltage-gated sodium channels: molecular substrates and contributions to channelopathies. *Cell Biochem Biophys* **35**, 171–190 (2001).

31. J. Silva, Slow inactivation of Na(+) channels. *Handb Exp Pharmacol* **221**, 33–49 (2014).

32. A. Stadnicka, W. M. Kwok, H. A. Hartmann, Z. J. Bosnjak, Effects of halothane and isoflurane on fast and slow inactivation of human heart hH1a sodium channels. *Anesthesiology* **90**, 1671–1683 (1999).

732 33. J.-H. Song, C.-S. Huang, K. Nagata, J. Z. Yeh, T. Narahashi, Differential Action of Riluzole on
733 Tetrodotoxin-Sensitive and Tetrodotoxin-Resistant Sodium Channels. *J Pharmacol Exp Ther* **282**,
734 707–714 (1997).

735 34. Y. Wang, J. Mi, K. Lu, Y. Lu, K. Wang, Comparison of Gating Properties and Use-Dependent Block
736 of Nav1.5 and Nav1.7 Channels by Anti-Arrhythmics Mexiletine and Lidocaine. *PLoS One* **10**,
737 e0128653 (2015).

738 35. D. Ren, *et al.*, A prokaryotic voltage-gated sodium channel. *Science* **294**, 2372–2375 (2001).

739 36. W. Ouyang, T.-Y. Jih, T.-T. Zhang, A. M. Correa, H. C. Hemmings Jr, Isoflurane inhibits NaChBac, a
740 prokaryotic voltage-gated sodium channel. *J Pharmacol Exp Ther* **322**, 1076–1083 (2007).

741 37. A. F. Barber, V. Carnevale, M. L. Klein, R. G. Eckenhoff, M. Covarrubias, Modulation of a voltage-
742 gated Na+ channel by sevoflurane involves multiple sites and distinct mechanisms. *Proceedings*
743 *of the National Academy of Sciences* **111**, 6726–6731 (2014).

744 38. R. M. Sand, K. J. Gingrich, T. Macharadze, K. F. Herold, H. C. Hemmings Jr, Isoflurane modulates
745 activation and inactivation gating of the prokaryotic Na+ channel NaChBac. *J Gen Physiol* **149**,
746 623–638 (2017).

747 39. S. G. Raju, A. F. Barber, D. N. LeBard, M. L. Klein, V. Carnevale, Exploring volatile general
748 anesthetic binding to a closed membrane-bound bacterial voltage-gated sodium channel via
749 computation. *PLoS Comput Biol* **9**, e1003090 (2013).

750 40. M. N. Kinde, *et al.*, Fluorine-19 NMR and computational quantification of isoflurane binding to
751 the voltage-gated sodium channel NaChBac. *Proc Natl Acad Sci U S A* **113**, 13762–13767 (2016).

752 41. D. Hollingworth, *et al.*, Structural basis for the rescue of hyperexcitable cells by the amyotrophic
753 lateral sclerosis drug Riluzole. *Nat Commun* **15**, 8426 (2024).

754 42. L. G. Sait, *et al.*, Cannabidiol interactions with voltage-gated sodium channels. *Elife* **9**, e58593
755 (2020).

756 43. A. Sula, *et al.*, A tamoxifen receptor within a voltage-gated sodium channel. *Mol Cell* **81**, 1160-
757 1169.e5 (2021).

758 44. J. Payandeh, T. Scheuer, N. Zheng, W. A. Catterall, The crystal structure of a voltage-gated
759 sodium channel. *Nature* **475**, 353–358 (2011).

760 45. J. Payandeh, D. L. Minor, Bacterial voltage-gated sodium channels (BacNaVs) from the soil, sea,
761 and salt lakes enlighten molecular mechanisms of electrical signaling and pharmacology in the
762 brain and heart. *J Mol Biol* **427**, 3–30 (2015).

763 46. T. M. Gamal El-Din, M. J. Lenaeus, N. Zheng, W. A. Catterall, Fenestrations control resting-state
764 block of a voltage-gated sodium channel. *Proc Natl Acad Sci U S A* **115**, 13111–13116 (2018).

765 47. V. Jayalakshmi, N. Rama Krishna, CORCEMA refinement of the bound ligand conformation within
766 the protein binding pocket in reversibly forming weak complexes using STD-NMR intensities.
767 *Journal of Magnetic Resonance* **168**, 36–45 (2004).

768 48. PubChem, 2-Chloro-1,1,1,3,3,3-hexafluoropropane. Available at:
769 https://pubchem.ncbi.nlm.nih.gov/compound/9894 [Accessed 25 September 2024].

770 49. S. Rocchio, *et al.*, Identifying dynamic, partially occupied residues using anomalous scattering.
771 *Acta Cryst D* **75**, 1084–1095 (2019).

772 50. H. Palsdottir, C. Hunte, Lipids in membrane protein structures. *Biochimica et Biophysica Acta*
773 *(BBA) - Biomembranes* **1666**, 2–18 (2004).

774 51. X. Pan, *et al.*, Comparative structural analysis of human Nav1.1 and Nav1.5 reveals mutational
775 hotspots for sodium channelopathies. *Proc Natl Acad Sci U S A* **118**, e2100066118 (2021).

776 52. K. F. Herold, *et al.*, Volatile anesthetics inhibit sodium channels without altering bulk lipid bilayer
777 properties. *J Gen Physiol* **144**, 545–560 (2014).

778 53. K. F. Herold, C. Nau, W. Ouyang, H. C. Hemmings Jr, Isoflurane Inhibits the Tetrodotoxin-
779 resistant Voltagegated Sodium Channel Nav1.8. *Anesthesiology* **111**, 591–599 (2009).

780 54. M. Rogers, N. Zidar, D. Kikelj, R. W. Kirby, Characterization of Endogenous Sodium Channels in
781 the ND7-23 Neuroblastoma Cell Line: Implications for Use as a Heterologous Ion Channel
782 Expression System Suitable for Automated Patch Clamp Screening. *Assay Drug Dev Technol* **14**,
783 109–130 (2016).

784 55. S. Cestèle, E. Schiavon, R. Rusconi, S. Franceschetti, M. Mantegazza, Nonfunctional NaV1.1
785 familial hemiplegic migraine mutant transformed into gain of function by partial rescue of
786 folding defects. *Proc Natl Acad Sci U S A* **110**, 17546–17551 (2013).

787 56. M. N. McCarroll, *et al.*, Zebrafish behavioural profiling identifies GABA and serotonin receptor
788 ligands related to sedation and paradoxical excitation. *Nat Commun* **10**, 4078 (2019).

789 57. M. N. McCarroll, *et al.*, A Multimodal, In Vivo Approach for Assessing Structurally and
790 Phenotypically Related Neuroactive Molecules. *ACS Chem. Neurosci.* (2024).

791 58. G. Winter, xia2: an expert system for macromolecular crystallography data reduction. *J Appl*
792 *Cryst* **43**, 186–190 (2010).

793 59. D. G. Waterman, *et al.*, Diffraction-geometry refinement in the DIALS framework. *Acta Cryst D*
794 **72**, 558–575 (2016).

795 60. P. R. Evans, G. N. Murshudov, How good are my data and what is the resolution? *Acta Cryst D*
796 **69**, 1204–1214 (2013).

797 61. A. J. McCoy, *et al.*, Phaser crystallographic software. *J Appl Crystallogr* **40**, 658–674 (2007).

798 62. P. Emsley, B. Lohkamp, W. G. Scott, K. Cowtan, Features and development of Coot. *Acta*
799 *Crystallogr D Biol Crystallogr* **66**, 486–501 (2010).

800 63. G. N. Murshudov, *et al.*, REFMAC5 for the refinement of macromolecular crystal structures. *Acta*
801 *Cryst D* **67**, 355–367 (2011).

802 64. D. Liebschner, *et al.*, Polder maps: improving OMIT maps by excluding bulk solvent. *Acta*
803 *Crystallogr D Struct Biol* **73**, 148–157 (2017).

804 65. PyMOL | pymol.org. Available at: https://pymol.org/2/ [Accessed 31 January 2024].

66. E. F. Pettersen, *et al.*, UCSF Chimera--a visualization system for exploratory research and analysis. *J Comput Chem* **25**, 1605–1612 (2004).

67. A. Thorn, G. M. Sheldrick, ANODE: anomalous and heavy-atom density calculation. *J Appl Crystallogr* **44**, 1285–1287 (2011).

68. A. Sula, *et al.*, The complete structure of an activated open sodium channel. *Nat Commun* **8**, 14205 (2017).

69. J.-M. DeKeyser, C. H. Thompson, A. L. George, Cryptic prokaryotic promoters explain instability of recombinant neuronal sodium channels in bacteria. *J Biol Chem* **296**, 100298 (2021).

70. O. Hamill, A. Marty, E. Neher, B. Sakmann, F. Sigworth, Improved patch-clamp techniques for high-resolution current recording from cells and cell-free membrane patches. *Pflugers Arch* **391**, 85-100 (1981).

71. K. Solt, E. I. Eger, D. E. Raines, Differential modulation of human N-methyl-D-aspartate receptors by structurally diverse general anesthetics. *Anesth Analg* **102**, 1407–1411 (2006).

72. O. Trott, A. J. Olson, AutoDock Vina: improving the speed and accuracy of docking with a new scoring function, efficient optimization, and multithreading. *J Comput Chem* **31**, 455–461 (2010).